Contents lists available at ScienceDirect

Transactions of Nonferrous Metals Society of China

36(2026) 323−336

www.tnmsc.cn

Advancing surface properties of Ni through electrodeposition of Mo coatings in molten $CaCl_2$−$CaMoO_4$

Xiao-tian CHENG [a,b], Xiao YANG [b,*]

[a] School of Materials Science and Engineering, Zhejiang University, Hangzhou 310058, China;

[b] Department of Materials Science and Engineering, Westlake University, Hangzhou 310030, China

Abstract: The molten $CaCl_2$−$CaMoO_4$ system was investigated, and the electrodeposition of protective Mo coatings on Ni plates was demonstrated. The results confirm the high solubility of solid $CaMoO_4$ and the electrochemical reactivity of MoO_4^{2-} ions in molten $CaCl_2$. The eutectic temperature and composition of the system are identified as 1021 K and 4.74 wt.% $CaMoO_4$, respectively. Under constant-current electrolysis conditions of −10 mA/cm^2 at 1123 K, uniform and dense Mo coatings are obtained on Ni plates with up to 90.31% efficiency. Increasing the current density raises the overpotential, leading to refined grains and decreased roughness. The Mo-coated Ni plate exhibits a significant improvement in hardness and corrosion resistance. Microhardness increases from HV 46.00 to HV 215.10 after coating, and the corrosion rate in a 20 wt.% NaCl solution at room temperature decreases to 0.1% that of the bare plate. These findings enhance our understanding of the molten $CaCl_2$–$CaMoO_4$ system and emphasize the potential of innovative Mo coating technologies.

Key words: molybdenum; nickel; calcium molybdate; calcium chloride; electrodeposition; hardness; corrosion

1 Introduction

Molybdenum (Mo) is favored for coatings in critical metallic components due to its exceptional properties at high temperatures. Industrial techniques for Mo coating on metal substrates mainly involve plasma spraying [1] and chemical vapor deposition [2]. These methods, while effective, are energy-intensive and can lead to environmental pollution. In response, alternative technologies for Mo coating have been explored, with electrodeposition emerging as a promising approach because of its environmental cleanness and procedural simplicity.

The electrodeposition of high-quality Mo coatings in aqueous solutions is hindered by oxyphilic property of Mo [3,4]. Molten fluxes thus present a more suitable choice for electrodeposition. KOYAMA et al [5] pioneered the successful electrodeposition of Mo on various metals using KF–$Na_2B_4O_7$–K_2MoO_4. Subsequent research has expanded on this foundation, exploring a variety of fluoride-bearing fluxes including KF−B_2O_3 [6−8], KF−$K_2B_4O_7$ [9], KF−$Li_2B_4O_7$ [10], KF−SiO_2 [11], among others [12−17], to enhance process efficiency. While fluoride-bearing molten fluxes can yield high-quality Mo coatings, their use presents challenges due to the corrosive and harmful nature of fluorides. In search of alternatives, researchers [18−20] have explored systems based on oxides and chlorides. For instance, CHERNYSHEV et al [18] successfully prepared uniform Mo coatings thicker than 50 μm on glassy carbon substrates in molten NaCl−KCl−$MoCl_3$ at 1053 K, with a current efficiency close to 100%. These studies demonstrate the potential for achieving high-quality Mo coatings with high

Corresponding author: *Xiao YANG, Tel: +86-15988139223, E-mail: yangxiao@westlake.edu.cn

https://doi.org/10.1016/S1003-6326(25)66967-6

Received 26 March 2024; accepted 7 January 2025

efficiency using fluoride-free fluxes. However, compared to fluorides, most chlorides are generally less effective in dissolving oxides, which necessitates the use of expensive and volatile compounds like $MoCl_3$, $MoCl_5$, or K_3MoCl_6 as precursors.

To overcome the limitation of using expensive and volatile compounds as precursors in molten chloride systems, research has shifted towards employing more stable and readily obtainable Mo oxides or molybdates. One approach involves utilizing molten chloride−oxide mixtures. To date, there have been only a few reports on the electrodeposition of high-quality Mo coatings in molten chlorides using Mo oxides or molybdates as the precursor. KOLOSOV et al [19] claimed the successful electrodeposition of Mo coatings on Ni in molten $CaCl_2$−CaO at 1190 K, using MoO_3 as the precursor. While their study demonstrates the feasibility of Mo coating in the $CaCl_2$-based molten flux, there is an opportunity to further enhance this process by using molten $CaCl_2$−$CaMoO_4$ instead. Notably, $CaMoO_4$, also known as powellite, occurs naturally in the Earth's crust, making it a readily available and sustainable precursor for electro-deposition. The use of molten $CaCl_2$−$CaMoO_4$ could simplify the process and facilitate the broad application of Mo coating technology.

However, there are certain knowledge gaps that need to be addressed. The dissolution behavior of solid $CaMoO_4$ in molten $CaCl_2$ is a critical subject that requires thorough investigation to understand its solubility and the factors that influence this process. Additionally, a deep insight into the electrochemical behavior of Mo(IV) within the melt, as well as the mechanisms that drive the formation of Mo coatings, is essential for optimizing this electrodeposition method. Although some reports in the literature touch upon related topics, a comprehensive investigation into the underlying mechanisms is still necessary.

The objective of this work is to investigate and demonstrate the feasibility of Mo coating on Ni plates through electrodeposition in molten $CaCl_2$−$CaMoO_4$. The study initially focuses on clarifying the fundamental aspects of the molten $CaCl_2$−$CaMoO_4$ system, including the dissolution behavior of solid $CaMoO_4$, the phase relationship within the system, and the electrochemical behavior of MoO_4^{2-}. The study also delves into the mechanisms underlying the formation of Mo coatings on Ni plates through electrodeposition. Additionally, the hardness and anti-corrosion performance of the Mo-coated Ni plates are investigated to evaluate the efficacy of the Mo coating in enhancing the properties of the Ni substrate. By clarifying these mechanisms and establishing the practicality of this method, the findings will provide crucial insights for advancing more efficient and sustainable Mo coating technologies.

2 Experimental

2.1 Materials

Reagent grade $CaCl_2$ (Greagent, 97%) and $CaMoO_4$ (Adamas, 99.9%) were used as the supporting electrolyte and the Mo precursor, respectively. To remove moisture, $CaCl_2$ was first subjected to a vacuum drying process at 473 K for 24 h, followed by another treatment at 773 K for 12 h. Figure S1 in Supplementary Materials (SM) shows the size distribution of $CaMoO_4$, with 90% of particles smaller than 10.7 μm. Ni plates (Hebei Qingyuan Metal Materials, purity 99.98%) with a thickness of 0.5 mm were used as the substrate for Mo coating.

2.2 Procedure

2.2.1 Dissolution

The experimental apparatus to study the dissolution behavior of solid $CaMoO_4$ in molten $CaCl_2$ is similar to that described in a previous study [21]. An Al_2O_3 crucible (Hubei Gude Tech., purity 99%, outer diameter 80 mm, inner diameter 70 mm, height 120 mm) containing approximately 220 g of $CaCl_2$ was set inside the sealed SiO_2 vessel (outer diameter 120 mm, inner diameter 112 mm, height 580 mm) with flowing Ar (200 mL/min) in a programmable crucible furnace. Once $CaCl_2$ was melted at the setting temperatures (1073, 1123, and 1173 K), a small Al_2O_3 crucible (outer diameter 60 mm, inner diameter 56 mm, height 22 mm), containing approximately 40 g of $CaMoO_4$, was carefully lowered into the melt. Over time, $CaMoO_4$ powder in the small crucible would gradually dissolve in $CaCl_2$ until saturation. The dissolution time was within 72 h. During this period, the melt outside the small crucible was periodically sampled

for chemical analysis by dipping an Al_2O_3 rod (diameter 6 mm) at nearly the same position. All collected samples were stored in a sealed glass bin to avoid moisture exposure before analysis.

2.2.2 Cooling curve measurement

Approximately 100 g of $CaCl_2$–$CaMoO_4$ mixtures were initially heated to a high temperature to ensure complete melting. Subsequently, a temperature decreasing program was initiated in the furnace to cool the melt at a rate of 5 K/min, allowing for the observation of phase transitions occurring in the melt. Throughout the cooling process, the temperature of the melt was continuously recorded using a K-type thermocouple connected to a data logger. Prior to this test, the thermocouple was calibrated to ensure accuracy. The calibration process involves the measurement of cooling curves for pure chlorides, including $MgCl_2$, $CaCl_2$, NaCl and CsCl. By analyzing the cooling curves, it becomes possible to identify the temperature at which solidification and phase transition occur in the molten $CaCl_2$–$CaMoO_4$ system.

2.2.3 Electrochemical test

Cyclic voltammetry (CV) test was conducted both in molten $CaCl_2$ and in molten $CaCl_2$–$CaMoO_4$ using an electrochemical workstation (Hokuto Denko, model HAG1232m, HZ−7000 series) in a three-electrode manner at 1123 K. The working electrode was a graphite rod (Shandong Guanzhi New Material Technology, purity 99.99%, diameter 3 mm, immersion depth in melt 1 mm). The counter electrode was a Mo plate (purity 99.95%, 25 mm × 5 mm × 1 mm, immersion depth in melt 20 mm). The reference electrode (Ag^+/Ag) was prepared by immersing an Ag wire (Runde Metal Materials, purity 99.9%, diameter 1 mm) in $CaCl_2$–0.5mol.%AgCl (Shanghai Titan Scientific, purity 98%). This assembly was enclosed in a SiO_2 tube (outer diameter 6 mm, inner diameter 5 mm, height 700 mm). The Ag^+/Ag potential was calibrated using the Cl_2/Cl^- potential estimated by CV test.

Initially, CV test was performed in pure molten $CaCl_2$ (200 g) to establish a baseline. Following that, powdery $CaMoO_4$ (1.08 g) was added to the melt and allowed to dissolve completely over a period of 2 h. After ensuring the complete dissolution of $CaMoO_4$, the melt was sampled for chemical analysis to determine the composition. Subsequently, CV test was conducted once more to investigate the electrochemical behavior of soluble Mo(VI) ions in the melt.

2.2.4 Electrodeposition

After conducting the CV test in molten $CaCl_2$–$CaMoO_4$, an additional amount of powdery $CaMoO_4$ (2.52 g) was added to the melt to increase the content of soluble Mo(VI) ions. Electrolysis was then performed in a two-electrode configuration at constant current density (−5, −10, −20 and −40 mA/cm^2; "–" indicates cathodic current). A Ni plate (purity 99.99%, 10 mm × 5 mm × 0.5 mm, immersion depth in melt 10 mm) was used as the working electrode (cathode). A Mo plate (25 mm × 5 mm × 1 mm, immersion depth in melt 20 mm) was used as the counter electrode (anode). Before usage, the Ni and Mo plates underwent ultrasonic cleaning in alcohol to remove any contaminants that could affect the electrode reactions. Once electrolysis was complete, the Ni plate was carefully removed from the melt and subjected to ultrasonic washing in distilled water. Subsequently, it was dried in preparation for further analysis and characterization to assess the quality and properties of the deposited material.

2.3 Measurement and characterization

The Mo content in the collected melt sample was measured using an inductively coupled plasma-atomic emission spectrometer (ICP-AES, ThermoFisher, ICAP PRO XP). The Raman spectroscopy measurements were conducted using a spectrometer (WITec, Alpha300R) with an excitation wavelength of 532 nm. The surface and cross-section morphologies of the Mo-coated Ni plates were examined by an analytical field emission scanning electron microscope (AFESEM, Gemini 450). Element analysis was performed using an energy dispersive X-ray spectrometer (EDS, Oxford, Ultim EXTREME,). The surface roughness was determined using an atomic force microscope (AFM, Bruker Dimension Icon). The phase composition of the coatings was characterized using powder X-ray diffraction (PXRD, Cu K_α, Bruker, D8 Advance). The Vickers hardness of the sample was measured using a microhardness tester (Innovatest, FALCON 507). The corrosion test was carried out at room temperature using a 20 wt.% NaCl solution, which was prepared by dissolving reagent grade NaCl in distilled water.

3 Results and discussion

3.1 Dissolution of solid $CaMoO_4$ in molten $CaCl_2$

Figure 1(a) shows the dissolution curves of solid $CaMoO_4$ in molten $CaCl_2$ at various temperatures. The corresponding raw data can be found in Table S1 of SM. The content of Mo gradually increases until reaching a plateau, indicating the dissolution of solid $CaMoO_4$ into the melt. Figure 1(b) shows the photographs comparing the appearance of pure $CaCl_2$ and the $CaCl_2$–$CaMoO_4$ mixture sampled at 1123 K. The dissolution of $CaMoO_4$ for 48 h transforms the melt from a colorless state to a milk-white color. The solubility of $CaMoO_4$ in molten $CaCl_2$, determined by averaging the contents of Mo(VI) or $CaMoO_4$ in the melt after dissolution for 40 h, increases with increasing temperature. Notably, at 1123 K, the solubility approaches 10 wt.% ($CaMoO_4$), indicating its soluble nature in molten $CaCl_2$. This property is beneficial for the electrodeposition of Mo coatings, as it creates favorable conditions for the process.

To clarify the dissolution mechanism, the molten $CaCl_2$–$CaMoO_4$(std.) melt sampled at 1123 K was rinsed with distilled water, and the remaining residues were subsequently analyzed. Additionally, the solid-state reaction between $CaMoO_4$ and $CaCl_2$ was studied by heating the mixtures (molar ratios of 5:1 and 1:1) at 1023 K for 5 h. The post-reaction substance was rinsed with distilled water to recover the water-insoluble residues. Figure 2(a) shows the XRD patterns of these residues, with only $CaMoO_4$ detected in all cases. The results indicate that solid $CaMoO_4$ does not react with molten $CaCl_2$ to form new compounds during its dissolution. This behavior of $CaMoO_4$ is distinct from that of other oxysalts such

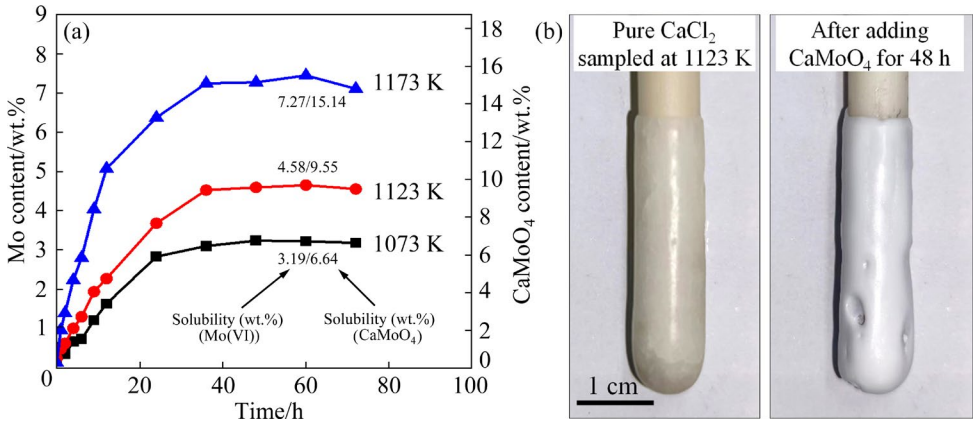

Fig. 1 (a) Dissolution curves of solid $CaMoO_4$ in molten $CaCl_2$ at different temperatures; (b) Photographs of sampled melts of pure $CaCl_2$ and after adding solid $CaMoO_4$ for 48 h at 1123 K

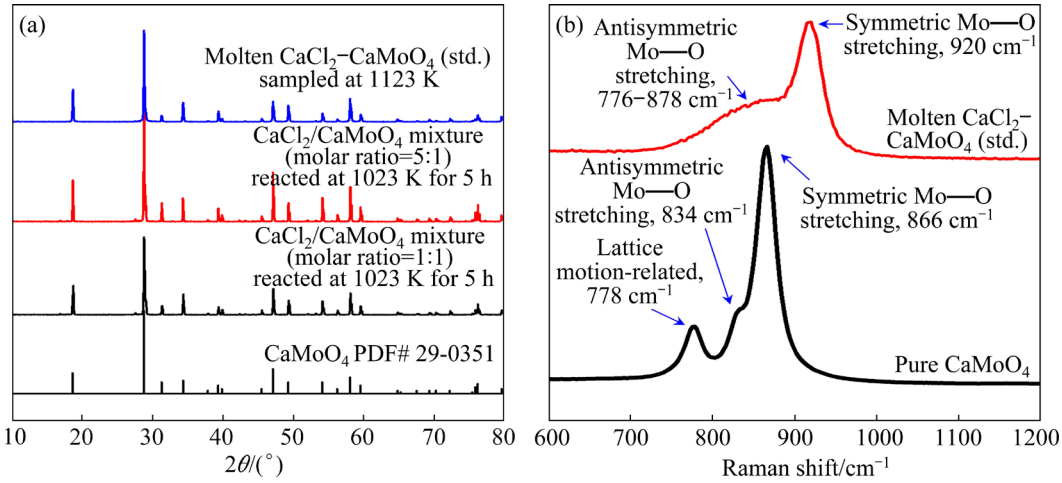

Fig. 2 (a) XRD patterns of water-rinsed residues of molten $CaCl_2$–$CaMoO_4$ (std.) sampled at 1123 K and $CaCl_2$/$CaMoO_4$ mixtures (molar ratios of 5:1 and 1:1) heated at 1023 K for 5 h; (b) In-situ Raman spectra of molten $CaCl_2$–$CaMoO_4$ (std.) and pure $CaMoO_4$ at 1123 K

as $Ca_3(PO_4)_2$ and $CaSiO_3$, which react with $CaCl_2$ to form oxymuriates like Ca_2PO_4Cl or $Ca_2SiO_3Cl_2$ [21,22].

Figure 2(b) shows the in-situ Raman spectrum of molten $CaCl_2$−$CaMoO_4$ (std.) at 1123 K, with pure solid $CaMoO_4$ at the same temperature serving as a reference. Pure $CaMoO_4$ exhibits three Raman bands within the analyzed frequency range. Based on the previous studies [23,24], these bands were identified as: the symmetric Mo−O stretching mode at 866 cm^{-1} and the antisymmetric Mo−O stretching mode at 834 cm^{-1} within the [MoO_4] clusters, and the lattice motion-related vibration mode at 778 cm^{-1}.

In the spectrum of molten $CaCl_2$−$CaMoO_4$ (std.), only two Raman bands are observed: an intense one at 920 cm^{-1} and a broad one spanning from 776 to 878 cm^{-1}. These bands are interpreted as originating from the symmetric and antisymmetric Mo−O stretching modes within the [MoO_4] clusters, respectively. The absence of the lattice motion-related vibration mode suggests the dissolution of solid $CaMoO_4$ in molten $CaCl_2$. This suggests that the [MoO_4] clusters remain intact in the melt, transitioning into mobile MoO_4^{2-} ions. Notably, both bands exhibit broadening, likely due to enhanced thermal motion and disorder within the MoO_4^{2-} ions in a molten state. The blue-shift of the symmetric Mo–O stretching mode is evident, which can be attributed to the influence of mobile Ca^{2+} and Cl^- ions in the melt. The interaction between MoO_4^{2-} and Ca^{2+} or Cl^- may alter the molecular environment, resulting in the blue-shift of the Raman band.

Based on these results, the dissolution mechanism of solid $CaMoO_4$ in molten $CaCl_2$ can be summarized. When solid $CaMoO_4$ comes into contact with molten $CaCl_2$, it undergoes direct dissociation into soluble ions (Ca^{2+} and MoO_4^{2-}) at the solid−liquid interface via

$$CaMoO_4(s) \rightarrow Ca^{2+}(\text{in melt}) + MoO_4^{2-}(\text{in melt}) \quad (1)$$

These ions then diffuse away from the interface into the broad volume of the molten salt. The dissociation and diffusion continue until the melt reaches a saturation with respect to MoO_4^{2-}. In a separate dissolution experiment, it was observed that the introduction of Ar bubbling in the melt enhanced the dissolution rate (Fig. S2 in SM). This suggests that the diffusion of MoO_4^{2-} ions in the melt, rather than the initial dissociation, could potentially be the rate-determining step in the overall dissolution process. Ar bubbling enhances mass transport by stirring the melt and likely thins the saturated boundary layer around the particles, accelerating the transfer of these ions into the bulk. A deep analysis into the dissolution kinetics and thermodynamics has been conducted, detailed in SM.

3.2 Phase relationship of $CaCl_2$−$CaMoO_4$ binary system

It is considered that $CaMoO_4$ and $CaCl_2$ will form a eutectic mixture. To determine the liquidus lines and the eutectic point of the $CaCl_2$−$CaMoO_4$ binary system, studies were conducted on the solubility of $CaMoO_4$ in $CaCl_2$ at various temperatures and the cooling curves for different compositions. Figure 3 shows the cooling curves from homogeneous melts with varying $CaMoO_4$ contents. The presence of inflection points on these curves, which occur due to the release of heat from the precipitation of the solute during cooling, marks the locations on the liquidus line.

Through analyzing these data, it becomes possible to clarify the phase relationship within the $CaCl_2$−$CaMoO_4$ binary system, particularly on the $CaCl_2$-rich side, as shown in Fig. 4. The eutectic point is identified as the intersection of the extension of the liquidus lines, determined from solubility and cooling data. The eutectic temperature and composition are established at 1021 K and 4.74 wt.% (or 2.69 mol.%) of $CaMoO_4$. It is important to note that $CaMoO_4$ does not form any compounds with $CaCl_2$, meaning that the solid phase within the two-phase region on the $CaMoO_4$-rich side consists solely of $CaMoO_4$. This clarification of the liquid region in the $CaCl_2$−$CaMoO_4$ binary system is necessary for designing molten salt compositions which facilitate efficient electrodeposition of Mo. Remarkably, this study represents the first reported instance of elucidating the phase relationship in the $CaCl_2$−$CaMoO_4$ binary system.

3.3 Electrochemical behavior of MoO_4^{2-}

The electrochemical behavior of MoO_4^{2-} on a graphite electrode in molten $CaCl_2$ was clarified through electrochemical tests. Figure 5(a) illustrates

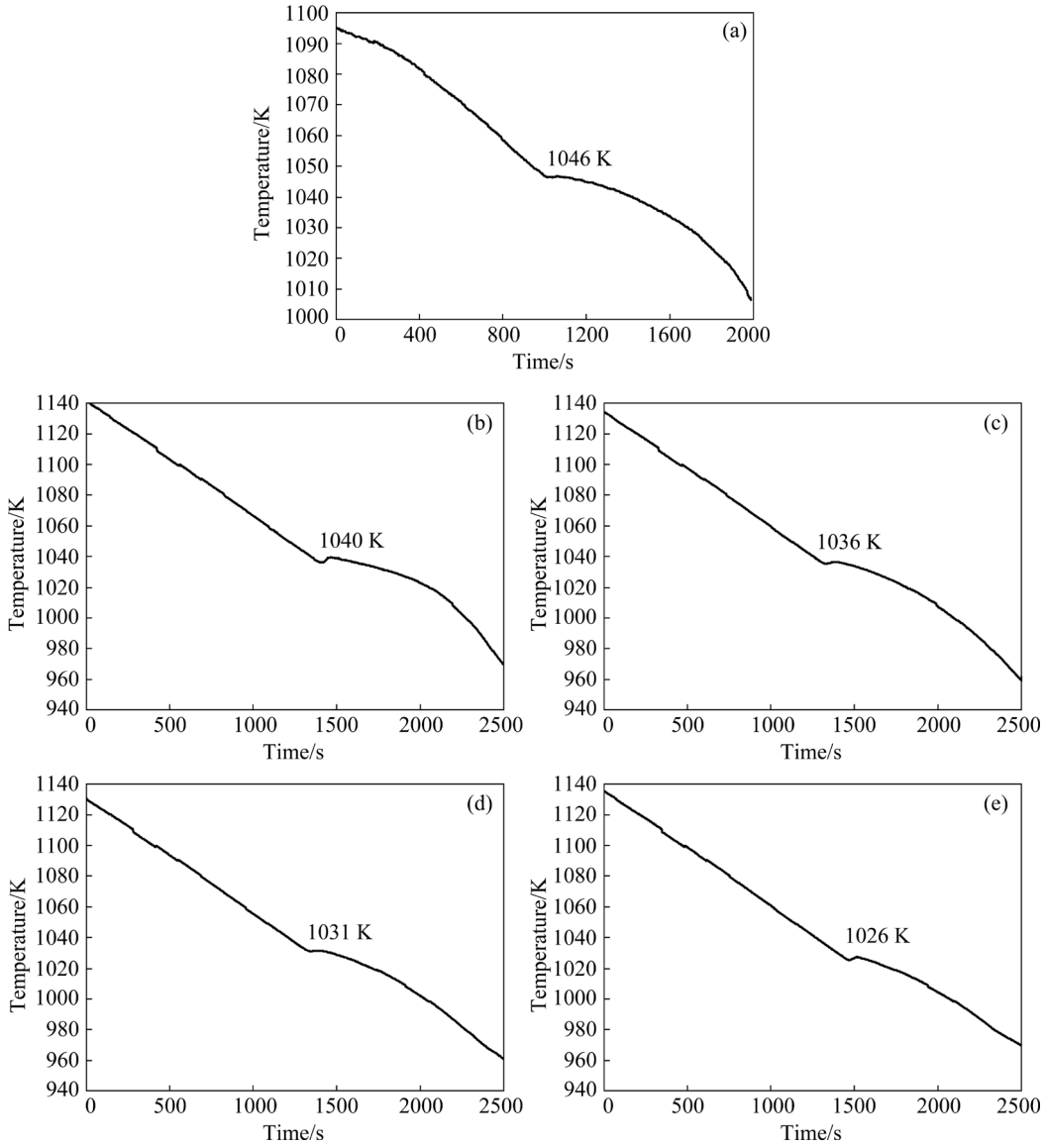

Fig. 3 Cooling curves obtained from molten $CaCl_2$–$CaMoO_4$ with varying compositions at cooling rate of 5 K/min: (a) Pure $CaCl_2$; (b) $CaCl_2$–0.98wt.%$CaMoO_4$; (c) $CaCl_2$–2.17wt.%$CaMoO_4$; (d) $CaCl_2$–2.87wt.%$CaMoO_4$; (e) $CaCl_2$–3.89wt.%$CaMoO_4$

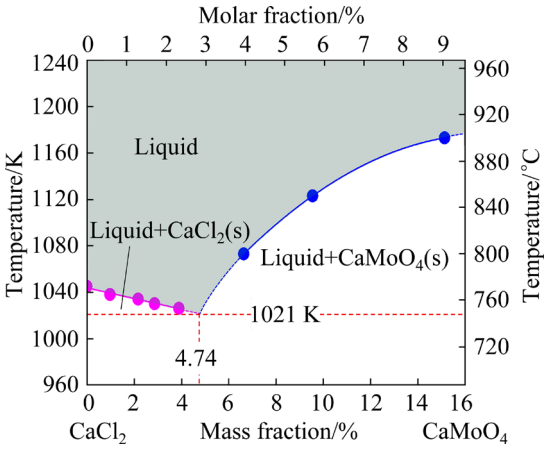

Fig. 4 Phase relationship in $CaCl_2$–$CaMoO_4$ binary system on $CaCl_2$-rich side

the cyclic voltammograms (CVs) obtained in pure $CaCl_2$ and in $CaCl_2$–0.52wt.%$CaMoO_4$ at 1123 K. In pure $CaCl_2$, as represented by the dotted line, only a single pair of cathodic and anodic peaks is evident. These peaks correspond to the electrochemical deposition and oxidation of Ca. However, upon the addition of 0.52wt.%$CaMoO_4$, new redox peaks emerge between −1.30 and −1.70 V (vs Cl_2/Cl^-), as indicated by the solid line.

The electrochemical reduction of Mo(VI) can be described as

$$MoO_4^{2-}\text{(in melt)}+6e\rightarrow Mo(s)+4O^{2-}\text{(in melt)} \quad (2)$$

Using the method described in a previous

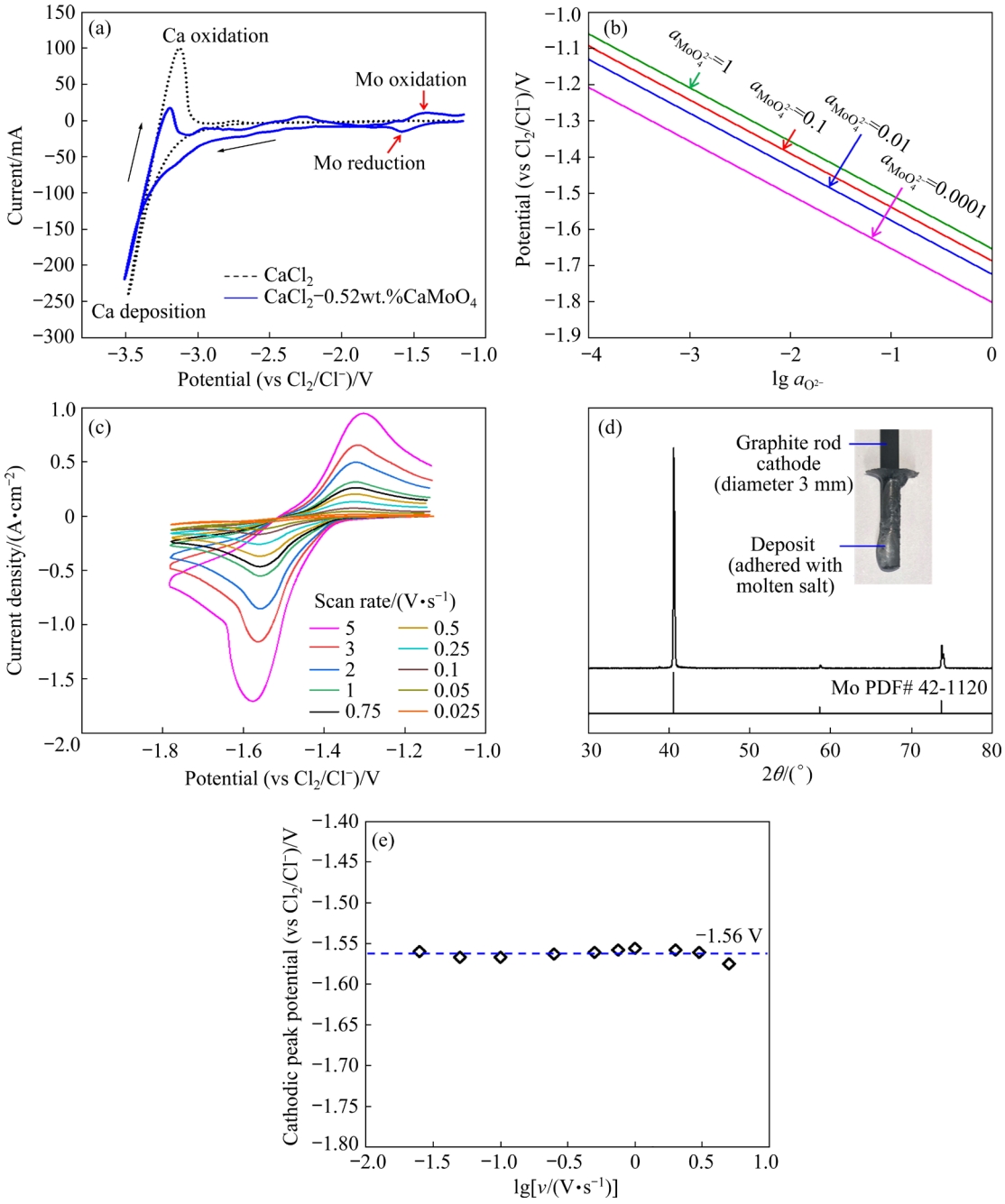

Fig. 5 (a) CVs at graphite electrode (diameter 3 mm, immersion depth in melt 1 mm) in pure $CaCl_2$ and in $CaCl_2$–0.52wt.%$CaMoO_4$ over broad potential range at 1123 K; (b) Relationship between equilibrium potential ($\varphi_{MoO_4^{2-}/Mo}$) and activity of MoO_4^{2-} ($a_{MoO_4^{2-}}$) or O^{2-} ($a_{O^{2-}}$); (c) CVs over narrow potential range with various scan rates (IR compensation: 80%); (d) XRD pattern of water-rinsed cathodic products after electrolysis at −1.60 V (vs Cl_2/Cl^-) for 5 min (Inset: Photograph of graphite cathode after electrolysis); (e) Dependence of cathodic peak potential on scan rate (lg v)

study [25], the equilibrium potential ($\varphi_{MoO_4^{2-}/Mo}$, vs Cl_2/Cl^-) at 1123 K can be calculated as

$$\varphi_{MoO_4^{2-}/Mo} = -1.65 + 0.037\lg a_{MoO_4^{2-}} - 0.15\lg a_{O^{2-}} \quad (3)$$

Figure 5(b) plots the relationship between $\varphi_{MoO_4^{2-}/Mo}$ and the activity of MoO_4^{2-} ($a_{MoO_4^{2-}}$) or O^{2-} ($a_{O^{2-}}$). The result indicates that the value of $\varphi_{MoO_4^{2-}/Mo}$ falls within the range of −1.06 to −1.80 V, depending on the values of $a_{MoO_4^{2-}}$ and $a_{O^{2-}}$. This suggests a strong possibility that the redox peaks between −1.30 and −1.70 V observed in Fig. 5(a) are associated with the electrochemical

reduction of MoO_4^{2-}.

Figure 5(c) shows the CV curves over a narrow potential range, with various potential scan rates from 0.025 to 5 V/s, providing a clear view of the electrochemical behavior. Within this range, a distinct cathodic peak is observed at around −1.56 V for each scan, paired with an anodic peak at −1.32 V. To further investigate the electrochemical process, electrolysis was conducted at −1.60 V (vs Cl_2/Cl^-) using a graphite electrode for 5 min (three-electrode manner). This results in the formation of solid deposits on the cathode. Subsequent XRD analysis of these deposits, as shown in Fig. 5(d), suggests the presence of elemental Mo. This finding supports the inference that the cathodic peaks on the CV curves are associated with the reduction of MoO_4^{2-} to Mo, while the anodic peaks likely represent the re-oxidation of the metal.

Figure 5(e) plots the relationship between the cathode peak potential and the logarithm of the scan rate (lg v). Within the range from 0.025 to 3 V/s, the cathode peak potential remains relatively stable at approximately −1.56 V (vs Cl_2/Cl^-). This stability indicates that the electrochemical reduction of MoO_4^{2-} to form elemental Mo is a reversible reaction within this scan rate range. However, as the scan rate increases to 5 V/s, the cathode peak potential shows a slight negative shift, suggesting that the electrochemical reaction becomes quasi-reversible or irreversible at high scan rates.

Figure 6(a) presents the chronopotentiograms obtained at a graphite electrode under various current densities , where each measurement exhibits a consistent potential platform ranging from −1.40 to −1.60 V (vs Cl_2/Cl^-). This potential platform corresponds to the electrochemical reduction of MoO_4^{2-}. It is worth noting that the reduction process from MoO_4^{2-} to Mo can be approximated as a one-step reaction. Therefore, the diffusion coefficient can be calculated using the Sand's equation [26]:

$$J\tau^{1/2} = -\frac{1}{2}nFC_{MoO_4^{2-}}(D_0\pi)^{1/2} \quad (4)$$

where J is the current density (A/cm^2); τ is the transition time (s); n is the number of electron transfer (n=6); F is the Faraday constant (96485 C/mol); $C_{MoO_4^{2-}}$ and D_0 are the molar concentration (mol/cm^3) and diffusion coefficient (cm^2/s) of MoO_4^{2-} ions in the melt, respectively. The methodology for determining the transition time is outlined in Fig. S5 in SM. Figure 6(b) plots the relationship between current density and the reciprocal of square root of the transition time. By examining the slope of the regression line, the diffusion coefficient of MoO_4^{2-} in molten $CaCl_2$−0.52wt.%$CaMoO_4$ at 1123 K is calculated to be 2.94×10^{-5} cm^2/s. This value is in the same order of magnitude as the result reported by JIN et al [17], who found a value of 0.91×10^{-5} cm^2/s in molten KF−MoO_3 at 1173 K. The comparability of these values suggests that MoO_4^{2-} ions exhibit similarly fast mass transfer behavior in molten $CaCl_2$ environments, even in the absence of fluorides.

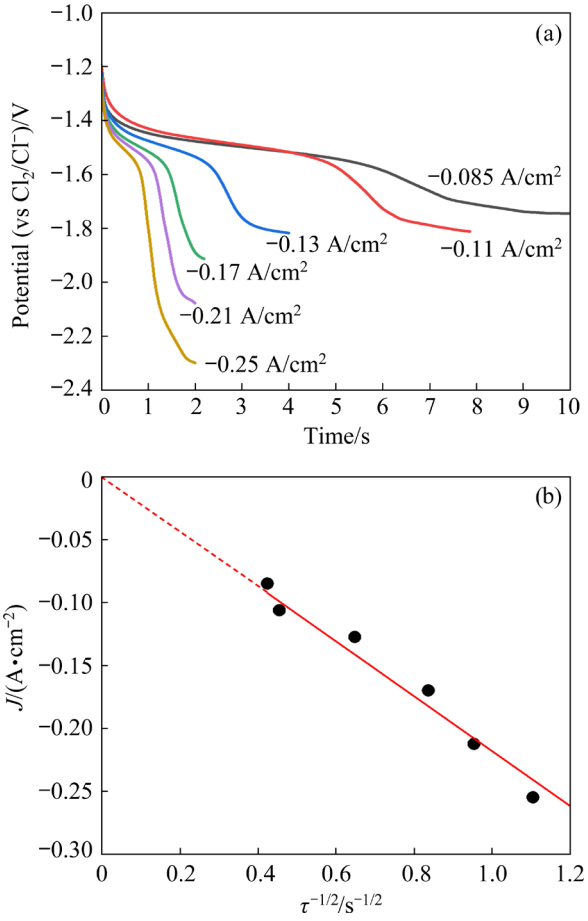

Fig. 6 (a) Chronopotentiograms at different current densities; (b) Relationship between current density and reciprocal of square root of transition time using graphite electrode (diameter 3.0 mm, immersion depth 1 mm) in molten $CaCl_2$−0.52wt.%$CaMoO_4$ at 1123 K

3.4 Electrodeposition of Mo coating

Constant current electrolysis was conducted in molten $CaCl_2$−1.61wt.%$CaMoO_4$ at 1123 K for electrodeposition on Ni plates. Figure 7 shows the SEM images of the surface and the cross-section of

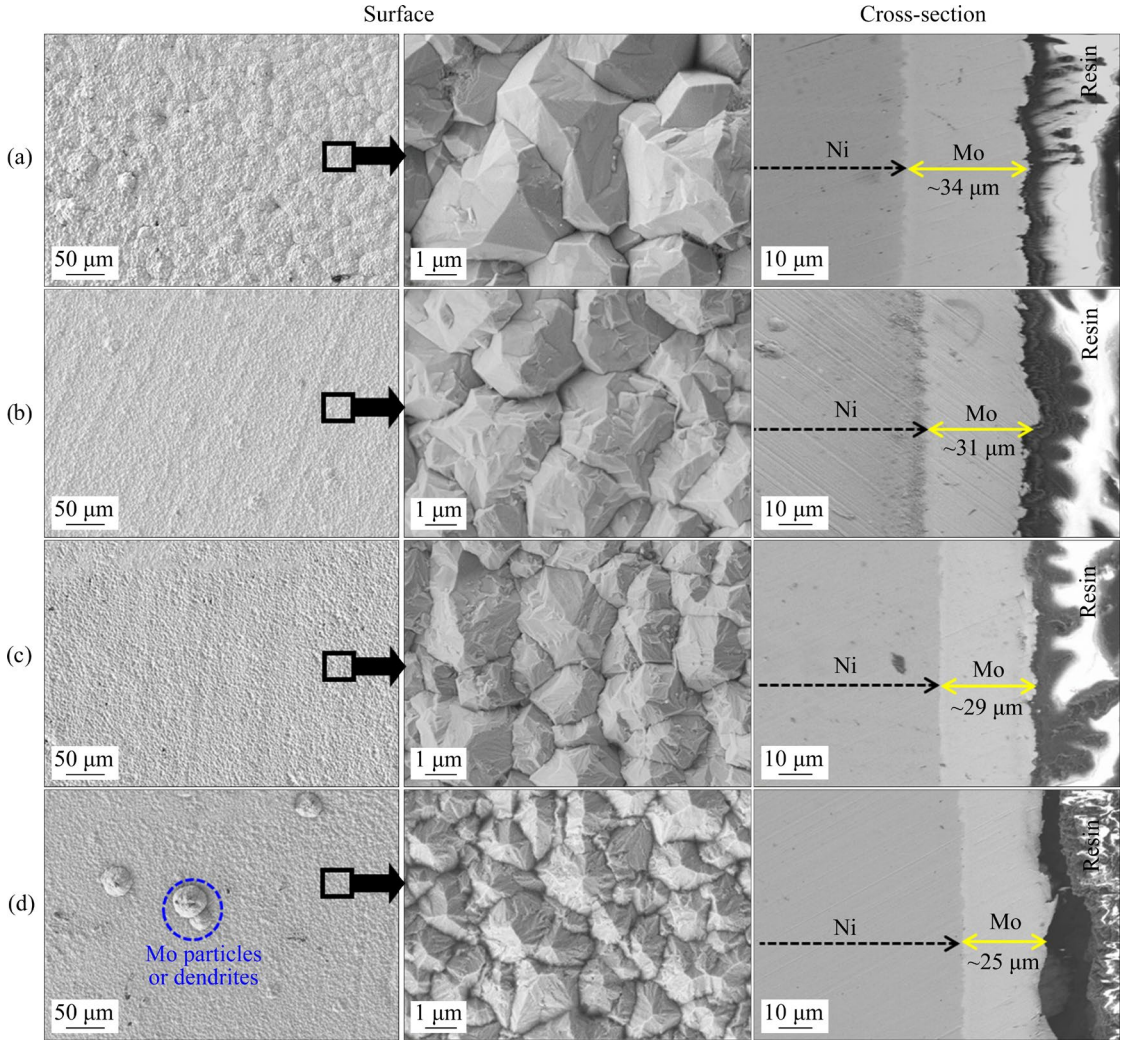

Fig. 7 SEM images of Mo-coated Ni plates after electrolysis at −5 mA/cm^2 for 10 h (a), −10 mA/cm^2 for 5 h (b), −20 mA/cm^2 for 2.5 h (c), and −40 mA/cm^2 for 1.25 h (d) in molten $CaCl_2$−1.61wt.%$CaMoO_4$ at 1123 K

the Mo-coated Ni plates. A consistent charge of 180 C was maintained in all experiments. The SEM and EDS analyses (refer to Fig. S6 in SM) confirm the deposition of Mo films on the Ni plates.

Given that the standard equilibrium potential of Ni ($\varphi^{\Theta}_{Ni^{2+}/Ni}$) in molten $CaCl_2$ at 1123 K is calculated to be −0.72 V (vs Cl_2/Cl^-), it is more positive than the standard reduction potential of MoO_4^{2-} ($\varphi^{\Theta}_{MoO_4^{2-}/Mo}$ =−1.65 V). Therefore, we believe that the formation of Mo is attributed to electrochemical reactions, rather than the thermal reduction by Ni. Variations in grain size, surface morphology, and coating thickness are noticeable among the samples according to the surface SEM images. An increase in current density from −5 to −40 mA/cm^2 leads to refinement in grain size, a phenomenon that can be explained using the theory of electrocrystallization. Additionally, AFM images in Fig. 8 illustrate that surface roughness decreases from 413 to 221 nm as the current density increases from −5 to −40 mA/cm^2, indicating that the surface becomes smoother at higher current densities.

The cross-section SEM images of the Mo-coated Ni plates exhibit dense and uniform coatings, free from any apparent voids or cracks, with a well-adhered boundary between the coating and substrate. These observations strongly suggest the successful deposition of Mo coating on Ni through electrolysis in molten $CaCl_2$. The result also shows a gradual decrease in coating thickness with the increase of current density. This is attributed to the formation of Mo particles or dendrites on the surface. Loose Mo particles become evident on the surface (Fig. S7 of SM), when the current density exceeds −10 mA/cm^2. Particularly at −40 mA/cm^2, a distinct dendrite

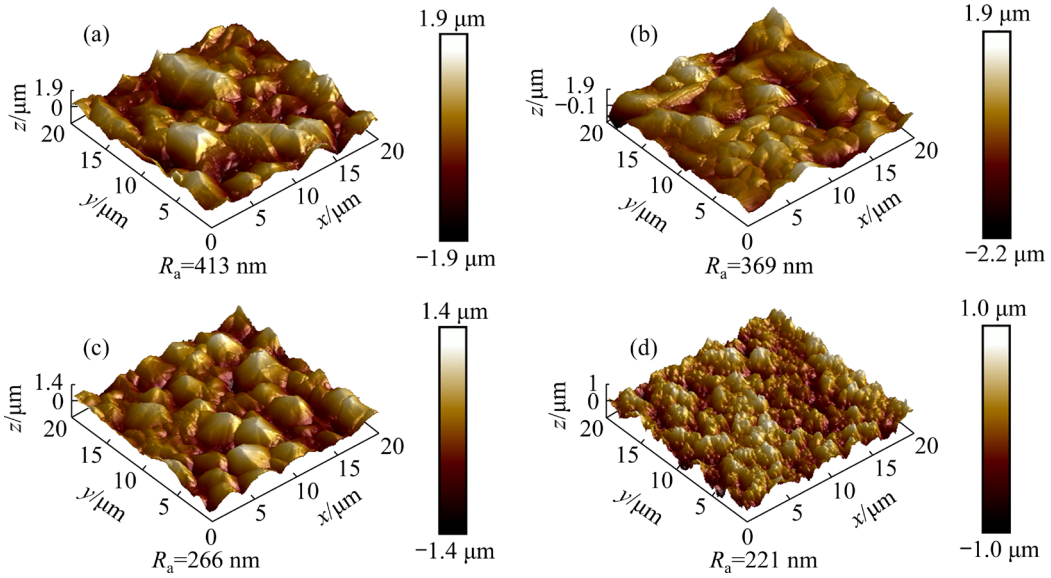

Fig. 8 Surface AFM images of Mo-coated Ni plates after electrolysis at −5 mA/cm^2 for 10 h (a), −10 mA/cm^2 for 5 h (b), −20 mA/cm^2 for 2.5 h (c), and −40 mA/cm^2 for 1.25 h (d) in molten $CaCl_2$−1.61wt.%$CaMoO_4$ at 1123 K (R_a means surface roughness)

structure (Fig. 7(d)) is observed. This phenomenon, known as the formation of particles or dendrites in electrodeposition, was originally proposed by FISCHER [27] on the growth of polycrystalline electrodeposits. As the current density increases, the electric field strength intensifies, leading to the creation of localized regions with high electric field concentration on the electrode surface where field lines converge. These regions with elevated electric field intensity facilitate the growth of powder or dendrites.

The formation of these undesirable Mo particles or dendrites leads to the decrease in process efficiency. In this study, the coating efficiency (η) is defined as

$$\eta = \frac{nF\Delta m}{MIt} \times 100\% \quad (5)$$

where M is the molar mass of Mo (M=96 g/mol); I and t are the applied current (A) and electrolysis time (s), respectively; Δm is the mass gain (g) of the Mo-coated Ni plate, measured after undergoing an ultrasonic rinse in distilled water and subsequent drying. This water rinse is intended to eliminate any removable particles or dendrites from the plate. Using Eq. (5), the coating efficiencies were calculated to be 90.64% at −5 mA/cm^2, 90.31% at −10 mA/cm^2, 73.84% at −20 mA/cm^2, and 70.17% at −40 mA/cm^2. These results show a decrease in coating efficiency with increasing current density, a trend consistent with the observed reduction in coating thickness. From the perspectives of energy consumption and coating quality, a lower current density (<−20 mA/cm^2) proves more favorable for producing dense and smooth Mo coatings. Additionally, even at the lowest current density of −5 mA/cm^2, the efficiency does not reach 100%. This could be attributed to Mo deposition on the current collector (Fig. S8 in SM) and impurity reactions in the melt.

Figure 9(a) depicts the XRD patterns of Mo-coated Ni plates over a wide range of current densities from −5 to −60 mA/cm^2. In all cases, the diffraction peaks of Mo are exclusively visible, confirming the successful formation of Mo coatings. Notably, there are clear variations in the relative intensities of these peaks. The predominant grain orientation of the Mo coating shifts from the (110) to the (211) plane as the current density increases. This change in grain orientation is quantitatively depicted in Fig. 9(b), which plots the relationship between the relative peak intensity ratio of (110) to (211) plane and the current density. The plot reveals that the ratio decreases with increasing current density. This trend suggests that it is possible to tailor the predominant grain orientation of Mo coatings in molten $CaCl_2$−$CaMoO_4$ by adjusting the electrolysis parameters. However, a comprehensive understanding of the underlying mechanisms requires further in-depth studies.

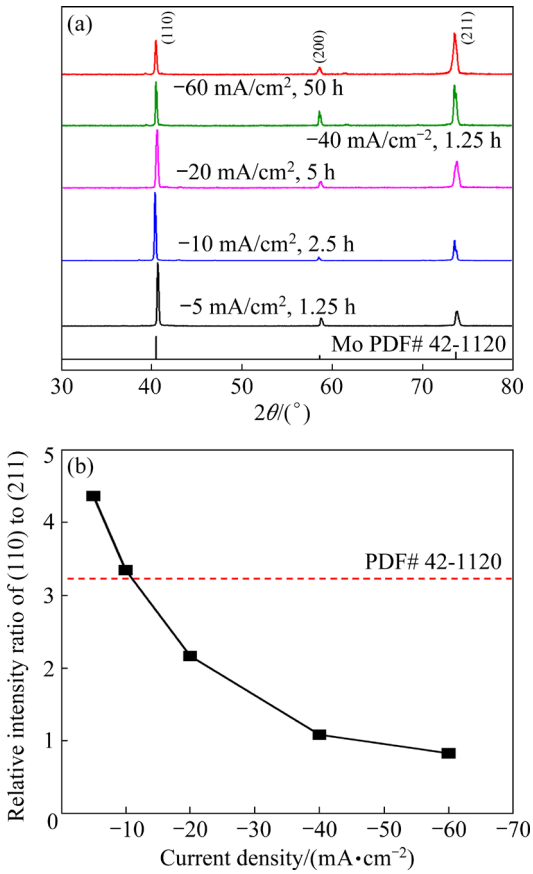

Fig. 9 (a) XRD patterns of Mo coatings electrodeposited under different current densities in molten $CaCl_2$–1.61wt.%$CaMoO_4$ at 1123 K; (b) Relationship between relative intensity ratio of (110) to (211) plane and current density

3.5 Properties of Mo-coated Ni plate

The Mo coating substantially enhances the hardness of the Ni substrate, as demonstrated by the Vickers microhardness testing results shown in Fig. 10. This figure compares the microhardness values of a bare Ni plate and Mo-coated samples, all of which were obtained through electrodeposition in molten $CaCl_2$–1.61wt.%$CaMoO_4$ at 1123 K. The result clearly demonstrates that the microhardness of the Mo-coated plate is higher than that of the bare Ni plate. Additionally, an increase in the current density for electrodeposition from −10 to −20 mA/cm^2 results in an increase of microhardness from HV 150.53 to HV 215.10. This phenomenon can be attributed to the influence of current density on the grain size of the Mo coating. As the current density increases, the grain size of the Mo coating decreases, leading to an increased number of grain boundaries. Based on the theory of dislocation [28], grain boundaries act as barriers to the movement of dislocations within the material. An increased number of grain boundaries intensifies the resistance to dislocation movement, making it more difficult for the material to deform under stress. Consequently, this increase in grain boundary density leads directly to an enhanced hardness of the Mo-coated plates.

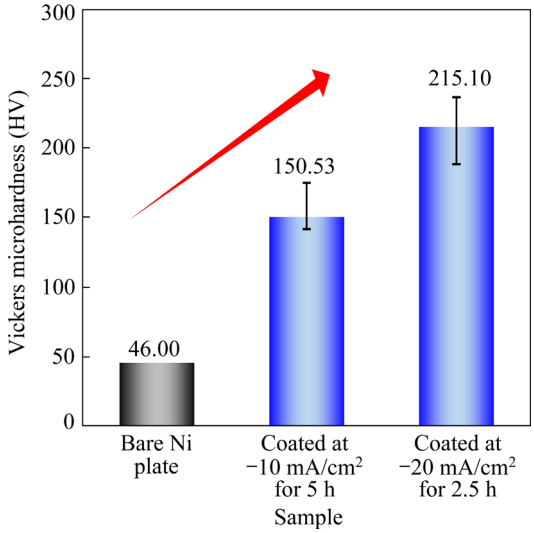

Fig. 10 Vickers microhardness of bare Ni plate and two Mo-coated Ni plates (obtained by electrodeposition at −10 mA/cm^2 for 5 h and −20 mA/cm^2 for 2.5 h in molten $CaCl_2$–1.61wt.%$CaMoO_4$ at 1123 K)

The Mo coating also improves the corrosion resistance of the Ni substrate. Figure 11 shows the corrosion morphology of a bare Ni plate and a Mo-coated sample (obtained by electrodeposition at −10 mA/cm^2 for 5 h in molten $CaCl_2$–1.61wt.%$CaMoO_4$ at 1123 K) before and after 96 h exposure to a 20 wt.% NaCl solution at room temperature under static conditions. The bare Ni plate exhibits severe local corrosion in the form of pitting. After 96 h corrosion test, the surface of bare Ni plate undergoes a substantial transformation from a clean and smooth appearance to one extensively covered with etch pits, indicative of significant material degradation (Fig. 11(a)). Surrounding these etch pits, loose corrosion products can be observed. EDS mapping analysis indicates a high content of O, pointing to the formation of nickel oxides. It is worth noting that these corrosion pits can act as initiation points for cracks, posing a risk of sudden fracture in the material. In contrast, the Mo-coated sample exhibits a surface morphology with negligible changes after the same exposure period (Fig. 11(b)). It maintains

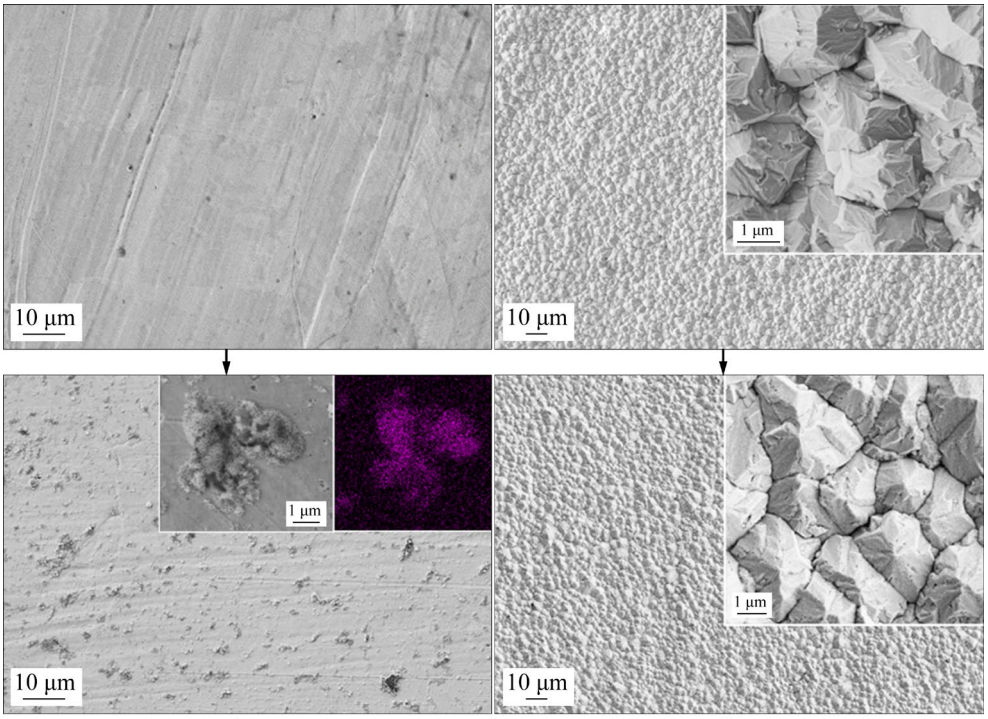

Fig. 11 Morphology of bare Ni plate (a) and Mo-coated Ni plate (b) (obtained by electrodeposition at −10 mA/cm^2 for 5 h in molten $CaCl_2$−1.61wt.%$CaMoO_4$ at 1123 K) before and after 96 h exposure to 20 wt.% NaCl solution at room temperature (Insets are SEM images at high magnification)

a smooth surface devoid of any visible signs of etch pits, suggesting that the Mo coating provides greater stability compared with bare Ni when exposed to corrosive environments.

Figure 12 shows the variation of Ni and Mo contents during exposure to the 20 wt.% NaCl solution at room temperature. For the bare Ni plate, the solution shows a rapid increase in Ni content, suggesting significant dissolution or corrosion of the plate. The average corrosion rate of the bare Ni plate within 96 h can be determined to be 1.4×10^{-3} mg/(h·cm^2). This reflects an active corrosion process where Ni from the plate is being steadily leached into the solution. In contrast, when the Mo-coated sample is tested, there is negligible change in Ni content in the solution. This suggests that Mo coating effectively prevents the dissolution of Ni. However, there is a slight increase in Mo content observed, which indicates some degree of Mo corrosion under the same conditions. The average corrosion rates of Mo and Ni for the Mo-coated Ni plate are determined to be 6.7×10^{-4} and 1.7×10^{-6} mg/(h·cm^2), respectively. Notably, the corrosion rate of Ni after Mo coating decreases to 0.1% that of the bare plate.

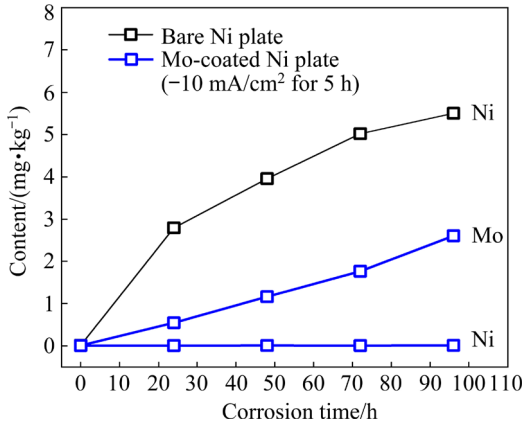

Fig. 12 Variation of Ni and Mo contents during exposure of bare Ni plate and Mo-coated Ni-plate (obtained by electrodeposition at −10 mA/cm^2 for 5 h in molten $CaCl_2$−1.61wt.%$CaMoO_4$ at 1123 K) to 20 wt.% NaCl solution at room temperature

This dramatic reduction highlights the effectiveness of the Mo coating in shielding the Ni substrate from corrosive agents. The Mo layer acts as a robust barrier, significantly minimizing the interaction between Ni and the corrosive environment, thus preserving the integrity of Ni substrate and substantially reducing its corrosion

loss. This protection mechanism is crucial for applications, where enhanced durability and longevity of Ni-based materials are required.

4 Conclusions

(1) Solid $CaMoO_4$ exhibits high solubility in molten $CaCl_2$, forming mobile and electrochemically reactive MoO_4^{2-} ions. The eutectic composition is determined under 4.74 wt.% $CaMoO_4$ at 1021 K.

(2) Electrochemical tests indicate that the reduction of MoO_4^{2-} is electrochemically reversible within the potential scan rate range from 0.025 to 3 V/s. The diffusion coefficient of MoO_4^{2-} is determined to be 2.94×10^{-5} cm^2/s at 1123 K.

(3) High-quality Mo coatings were successfully deposited on Ni plates through electrodeposition using molten $CaCl_2$−$CaMoO_4$. Operating at −10 mA/cm^2 for 5 h at 1123 K produces a 32 μm-thick Mo film with an efficiency of 90%. Higher current densities lead to grain refinement and decrease surface roughness, although they also lower the efficiency due to the formation of particles or dendrites.

(4) The Mo-coated Ni plates exhibit substantial improvements in hardness and anti-corrosion properties. Microhardness increases from HV 46.00 for a bare Ni plate to HV 215.10 after coating. The corrosion rate in a 20 wt.% NaCl solution at room temperature decreases to 0.1% that of the bare plate, highlighting the protective efficacy of Mo coating.

CRediT authorship contribution statement

Xiao-tian CHENG: Data curation, Investigation, Formal analysis, Writing − Original draft; **Xiao YANG:** Conceptualization, Methodology, Funding acquisition, Resources, Writing − Review & editing.

Declaration of competing interest

The authors declare that they have no known competing financial interests or personal relationships that could have appeared to influence the work reported in this paper.

Declaration of Generative AI and AI-assisted technologies in the writing process

During the preparation of this work the author(s) used Poe software to polish the language in this manuscript.

Acknowledgments

The authors appreciate Dr. Zhong CHEN from Instrumentation and Service Center for Molecular Sciences at Westlake University for the assistance in the Raman measurement, and thank Dr. Lin LIU, Mr. Wen-jing CAO and Dr. Xiao-he MIAO from Instrumentation and Service Center for Physical Sciences at Westlake University for the SEM, PXRD and SEM measurement, respectively. This work was supported by Research Center for Industries of the Future (No. WU2022C034) at Westlake University, China.

Supplementary Materials

Supplementary Materials in this paper can be found at: https://tnmsc.csu.edu.cn/download/22-p0323-2024-0468-Supplementary_Materials.pdf.

References

[1] YAN Jian-hui, HE Zhe-yu, WANG Yi, QIU Jing-wen, WANG Yue-ming. Microstructure and wear resistance of plasma-sprayed molybdenum coating reinforced by $MoSi_2$ particles [J]. Journal of Thermal Spray Technology, 2016, 25: 1322−1329.

[2] BEAUX M F II, VODNIK D R, PETERSON R J, BENNETT B L, SALAZAR J J, HOLESINGER T G, KING G, MALOY S A, DEVLIN D J, USOV I O. Chemical vapor deposition of Mo tubes for fuel cladding applications [J]. Surface and Coatings Technology, 2018, 337: 510−515.

[3] HASAN S N, XU M, ASSELIN E. Electrosynthesis of metallic molybdenum from water deficient solution containing molybdate ions and high concentrations of acetate [J]. Surface and Coatings Technology, 2019, 357: 567−574.

[4] SYED R, GHOSH S K, SASTRY P U, SHARMA G, HUBLI R C, CHAKRAVARTTY J K. Electrodeposition of thick metallic amorphous molybdenum coating from aqueous electrolyte [J]. Surface and Coatings Technology, 2015, 261: 15−20.

[5] KOYAMA K, HASHIMOTO Y, OMORI S, TERAWAKI K. Electrodeposition of molybdenum in KF−$Na_2B_4O_7$−K_2MoO_4 fused salts [J]. Transactions of the Japan Institute of Metals, 1984, 25: 265−275.

[6] KOYAMA K, HASHIMOTO Y, OMORI S, TERAWAKI K. Electrodeposition of molybdenum in KF−B_2O_3−K_2MoO_4 fused salts [J]. Transactions of the Japan Institute of Metals, 1984, 25: 804−809.

[7] KOYAMA K, HASHIMOTO Y, OMORI S, TERAWAKI K. Electrodeposition of molybdenum in KF−B_2O_3−Na_2MoO_4 fused salts [J]. Transactions of the Japan Institute of Metals, 1985, 26: 198−203.

[8] TERIWAKI K, KOYAMA K, HASHIMOTO Y, OMORI S. Electrodeposition of molybdenum in KF−B_2O_3−MoO_3 fused salts [J]. Journal of The Japan Institute of Metals, 1986, 50: 303−307.

[9] KOYAMA K, HASHIMOTO Y, TERAWAKI K. Smooth electrodeposits of molybdenum from KF−$K_2B_4O_7$−K_2MoO_4 fused salt melts [J]. Journal of the Less Common Metals, 1987, 134: 141−151.

[10] KOYAMA K, HASHIMOTO Y, TERAWAKI K. Smooth

electrodeposits of molybdenum from KF−$Li_2B_4O_7$−Li_2MoO_4 fused salt melts [J]. Journal of the Less Common Metals, 1987, 132: 57−67.
[11] ZATKO P, MAKYTA M, SYKOROVA J, SILNY A. Electrodeposition of molybdenum from KF−K_2MoO_4−SiO_2 melts [J]. Retrospective Collection, 1994, 48: 10−14.
[12] NAKAJIMA H, NOHIRA T, HAGIWARA R. Electrodeposition of metallic molybdenum films in $ZnCl_2$−NaCl−KCl−$MoCl_3$ systems at 250 °C [J]. Electrochimica Acta, 2006, 51: 3776−3780.
[13] KOU Qian, JIN Wei-liang, GE Chun-tao, PANG Jie, ZHANG Jun, HAARBERG G M, XIAO Sai-jun, WANG Ping. Preparation of molybdenum coatings by molten salt electrodeposition in Na_3AlF_6−NaF−Al_2O_3−MoO_3 system [J]. Coatings, 2023, 13: 1266.
[14] TAKEDA O, WATANABE S, ISEKI C, LU Xin, ZHU Hong-min. Influence of B-containing compound on electrodeposition of Mo and W in molten fluoride-oxide electrolyte [J]. Journal of the Electrochemical Society, 2022, 169: 122503.
[15] ENE N, DONATH C. Texture of electrolytic Mo deposition from molten alkali halide [J]. Journal of Optoelectronics and Advanced Materials, 2006, 8: 708−711.
[16] GHOSH S K, VARSHNEY J, SRIVASTAVA A, SRIVASTAVA C. Electrochemical investigation of cathodic deposition of Mo coating from oxofluoride molten salt and characterization [J]. Journal of the Electrochemical Society, 2021, 168: 046502.
[17] JIN Wei-liang, GE Chun-tao, KOU Qian, JIANG Peng-fei, XIAO Sai-jun. Electrochemical preparation of molybdenum coatings on nickel from KF−MoO_3 melts [J]. International Journal of Electrochemical Science, 2021, 16: 210311.
[18] CHERNYSHEV A A, APISAROV A P, ISAKOV A V, SHMYGALEV A S, ARKHIPOV S P, ZAIKOV Y P. Molybdenum electrodeposition in NaCl−KCl−$MoCl_3$ melt using pulse electrolysis [J]. Materials Chemistry and Physics, 2023, 298: 127475.
[19] KOLOSOV V N, KARPENKO O A, GEL R P, DROBOTENKO G A, SHEVYREV A A. Electrodeposition of high-purity molybdenum coatings on nickel1 [J]. Inorganic Materials, 2001, 37: 1263−1269.
[20] KOYAMA K, IGUCHI M. Smooth electrodeposition of molybdenum from oxide melts [J]. Denki Kagaku Oyobi Kogyo Butsuri Kagaku, 1995, 63: 161−163.
[21] CHENG Xiao-tian, YANG Xiao. Dissolution of calcium silicates in molten $CaCl_2$ [J]. Metallurgical and Materials Transactions B, 2023, 54: 192−202.
[22] ZHONG Yu-xiang, LIU Guan-ting, YANG Xiao. Isolating elemental phosphorus from sewage sludge ash by electrochemistry [J]. Resources, Conservation and Recycling, 2023, 190: 106815.
[23] WANG Min, WANG Chang-hao, WANG Jian, LU Li-ming, GONG Xiao-ye, TANG Xiao-hui, ZHANG Fu, YOU Jing-lin. Temperature-dependent Raman spectroscopic study of the double molybdate $KBi(MoO_4)_2$ [J]. Materials, 2020, 13: 5453.
[24] SINHA E, YADAV P. Study of structural and optical properties of $CaMoO_4$ ceramic synthesized by solid state reaction route [J]. Ferroelectrics, 2017, 517: 1−7.
[25] CHENG Xiao-tian, YANG Xiao. Electrochemical silicification of Mo in molten $CaCl_2$−$CaSiO_3$ enhances high-temperature oxidation resistance [J]. Corrosion Science, 2024, 227: 111746.
[26] SAND H J S. On the concentration at the electrodes in a solution, with special reference to the liberation of hydrogen by electrolysis of a mixture of copper sulphate and sulphuric acid [J]. Processings of the Physical Socieity of London, 1899, 17: 496.
[27] FISCHER H. Elektrolytische abscheidung und elektrokristallisation von metallen [M]. Berlin, Heidelberg: Springer, 1954.
[28] ANDERSON P M, HIRTH J P, LOTHE J. Theory of dislocations [M]. New York: Cambridge University Press, 2017.

熔融 $CaCl_2$−$CaMoO_4$ 中电沉积 Mo 涂层强化 Ni 基板表面性能

程肖甜[1,2]，杨 肖[2]

1. 浙江大学 材料科学与工程学院，杭州 310058；
2. 西湖大学 材料科学与工程系，杭州 310030

摘 要：对熔融 $CaCl_2$−$CaMoO_4$ 体系进行了研究，并利用该体系验证了在 Ni 基板上电沉积制备 Mo 涂层的可行性。研究发现了固体 $CaMoO_4$ 在熔融 $CaCl_2$ 中的高溶解特性以及 MoO_4^{2-} 离子在熔融 $CaCl_2$ 中的电化学活性。$CaCl_2$−$CaMoO_4$ 二元熔盐体系的共晶温度为 1021 K，共晶成分为 4.74%(质量分)$CaMoO_4$。在 1123 K 温度和 −10 mA/cm^2 恒电流条件下，在 Ni 基板上获得了均匀致密的 Mo 涂层，成膜效率达到了 90.31%。提高电流密度导致过电位增大，促进 Mo 涂层的晶粒细化，并降低表面粗糙度。表面 Mo 涂层的制备显著提升了镀钼镍板的硬度和耐腐蚀性能，材料显微硬度从 HV 46.00 提高到 HV 215.10。在室温条件下，在 20% NaCl(质量分数)溶液中，Ni 的腐蚀速率降低至初始基板的 0.1%。这些研究结果不仅加深了对 $CaCl_2$−$CaMoO_4$ 体系的理解，也显示了 Mo 涂层技术的应用潜力。

关键词：钼；镍；钼酸钙；氯化钙；电沉积；硬度；腐蚀

(Edited by Xiang-qun LI)